RESEARCH ARTICLE

ADVANCED ENERGY MATERIALS
www.advenergymat.de

Operando Tracking of Resistance, Thickness, and Mass of $Ti_3C_2T_x$ MXene in Water-in-Salt Electrolyte

Audrey Perju, Danzhen Zhang, Ruocun John Wang, Pierre-Louis Taberna, Yury Gogotsi,* and Patrice Simon**

MXenes are among the fastest-growing families of 2D materials, promising for high-rate, high-energy energy storage applications due to their high electronic and ionic conductivity, large surface area, and reversible surface redox ability. The $Ti_3C_2T_x$ MXene shows a capacitive charge storage mechanism in diluted aqueous LiCl electrolyte while achieving abnormal redox-like features in the water-in-salt LiCl electrolyte. Herein, various *operando* techniques are used to investigate changes in resistance, mass, and electrode thickness of $Ti_3C_2T_x$ during cycling in salt-in-water and water-in-salt LiCl electrolytes. Significant resistance variations due to interlayer space changes are recorded in the water-in-salt LiCl electrolyte. In both electrolytes, conductivity variations attributed to charge carrier density changes or varied inter-sheet electron hopping barriers are detected in the capacitive areas, where no thickness variations are observed. Overall, combining those *operando* techniques enhances the understanding of charge storage mechanisms and facilitates the development of MXene-based energy storage devices.

1. Introduction

MXenes are a family of 2D materials that have attracted significant attention[1] due to their metallic and ionic conductivity,[2] excellent mechanical properties,[3–5] and a variety of structures and compositions.[6] Among MXenes, the titanium carbide $Ti_3C_2T_x$ (with T being = O, —OH, —Cl, or —F termination groups and x the number of groups) stands out as one of the most extensively studied compositions, exhibiting remarkably high conductivity ranging over 20 000 S cm^{-1}.[7–10] Its properties make $Ti_3C_2T_x$ suitable for diverse applications, including energy storage, where it can serve as an active material for electrochemical capacitors,[11,12] as an anode for Li-ion and Na-ion batteries,[11–13] as a current collector,[14] or as a conductive binder.[15] $Ti_3C_2T_x$ is also used in electrochemical actuators,[16,17] tunable electromagnetic interference shielding,[9,18–20] and implantable and epidermal electrodes,[21–23] where the effects of ion transport and intercalation on electrical properties are of importance.

When used as an electrode material for energy storage applications, $Ti_3C_2T_x$ shows very different behaviors depending on the nature of the electrolyte. In acidic electrolytes, $Ti_3C_2T_x$ exhibits a complex electrochemical behavior based on redox charge transfer, rising from the interaction between protons and the oxygen terminations of the MXene.[24,25] However, only the double-layer capacitive charge storage is typically observed in neutral aqueous and organic electrolytes.[26–28] Challenges facing $Ti_3C_2T_x$ in aqueous electrolytes include the low-potential redox of titanium and the electrochemical stability potential window of water. The operating potential range of $Ti_3C_2T_x$ can be widened by utilizing Water-in-salt (WIS) electrolytes due to the strongly associated water.[29–38] Recently, an anomaly in the charging/discharging mechanism of $Ti_3C_2T_x$ in WIS LiCl has been reported.[29–39] It is characterized by current peaks in the cyclic voltammograms, attributed to surface-controlled redox-like processes with only partial charge transfer during Li$^+$ ions intercalation/deintercalation. Note that the negatively charged $Ti_3C_2T_x$ surface, in line with a positive Potential of Zero Charge (PZC), only allows for cation intercalation—in the present case, Li$^+$ ions.[29–33] Those current peaks have been reported as related to the intercalation of solvated Li$^+$ ions.[29–39] This distinctive behavior of the $Ti_3C_2T_x$ MXene, only observed in WIS electrolytes, constitutes an intriguing system requiring additional research to be fully understood.

In this work, we explored the charging/discharging mechanism of $Ti_3C_2T_x$ in both WIS LiCl and Salt-In-Water (SIW) diluted LiCl using a set of *operando* techniques. The in-plane

A. Perju, P.-L. Taberna, P. Simon
Université de Toulouse III Paul Sabatier
Laboratoire CIRIMAT
UMR CNRS 5085, 118 Route de Narbonne, Cedex 9, Toulouse 31062, France
E-mail: pierre-louis.taberna@univ-tlse3.fr; patrice.simon@univ-tlse3.fr

A. Perju, P.-L. Taberna, P. Simon
Réseau sur le Stockage Electrochimique de l'Energie (RS2E) FR CNRS
Amiens 3459, France

D. Zhang, R. J. Wang, Y. Gogotsi
A. J. Drexel Nanomaterials Institute
and Department of Materials Science and Engineering
Drexel University
Philadelphia, PA 19104, USA
E-mail: gogotsi@drexel.edu

The ORCID identification number(s) for the author(s) of this article can be found under https://doi.org/10.1002/aenm.202405028

DOI: 10.1002/aenm.202405028

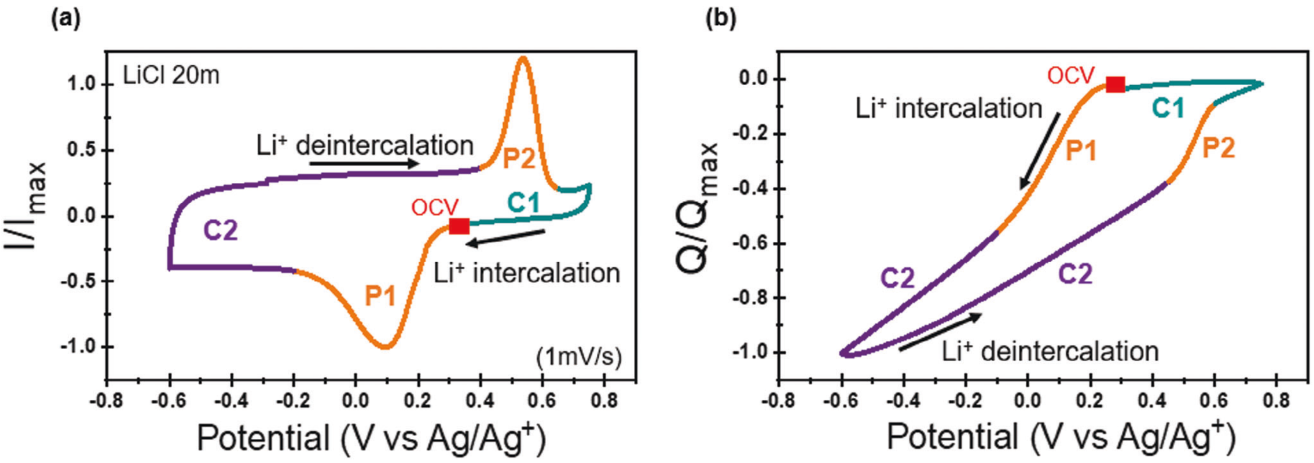

Figure 1. a) Cyclic voltammogram of a $Ti_3C_2T_x$ freestanding film at 1 mV s^{-1}, in 20 M LiCl, recorded in the in-plane resistance measurement cell. The OCV is indicated with the red square, and the different regions mentioned in the text are also identified in the figure. The current is normalized to the absolute maximum cathodic value. b) Normalized charge plotted versus potential, calculated from the CV displayed in (a). The OCV is indicated with the red square, and the different regions mentioned in the text are also identified in the figure. The charge is normalized to the maximum value.

resistance measurement technique, reported in our recent work,[40,41] has been employed to investigate the MXene resistance variations while undergoing cyclic voltammetry; an ElectroChemical Dilatometry (ECD) setup has been used to monitor the displacement along the *z*-axis (electrode thickness variations) under the same potential conditions; and Electrochemical Quartz Microbalance with Admittance monitoring (EQCM-A) analysis was performed to track mass changes during cycling. Integrating these diverse sources of information provides a broader picture of the physical changes of the MXene electrodes during Li⁺ ions intercalation/deintercalation.

2. Results and Discussion

2.1. $Ti_3C_2T_x$ in the WIS Electrolyte

Cyclic voltammetry (CV) of a $Ti_3C_2T_x$ free-standing film, prepared according to the protocol reported by Mathis et al.[8] (also described in the Experimental Procedures Section), conducted in 20 M LiCl (WIS) electrolyte using the in-plane resistance measurements cell, is shown in **Figure** 1a. The experimental setup allowing in-plane resistance measurements is identical to the one described in our previous work,[40,41] and is further elucidated in Figure S1 (Supporting Information). In Figure 1a, the current was normalized to the absolute value of the maximum cathodic current. The dimensionless charge (Q/Q_{max}) is plotted against the potential in Figure 1b. Three distinct regions are discernible within the voltammogram and are highlighted in Figure 1a,b.

Starting from the fully delithiated state at 0.75 V versus Ag/Ag⁺ and beginning the lithium intercalation by applying a decreasing potential, it is possible to identify a first region (C1) ranging from 0.75 to 0.3 V versus Ag/Ag⁺, where only a small current is recorded. C1 corresponds to the capacitive adsorption of cations onto the surface of the MXene sheet.[29,33,39]

Subsequently, a current peak (P1) appears at around 0.1 V versus Ag/Ag⁺. Following the peak, as lithium insertion proceeds from −0.2 to −0.6 V versus Ag/Ag⁺, a second capacitive region labeled as C2 emerges within this potential range. Consistent with the previously reported CV of this system,[29,39] the capacitive current within the C2 region exceeds that of C1, indicating enhanced charge storage following the current peak (Figure 1a). Moreover, as depicted in Figure 1b, the total charge in the region C2 is higher than C1, illustrating an augmented charge storage process.

This observation underscores the possibility of an "activation" mechanism happening at the peak potential, leading to the enhancement of lithium intercalation. This activation of the charge storage is most likely due to entering the nondesolvated Li⁺ ions, increasing the *d*-spacing and leading to partial charge transfer (weak surface redox).[29,39] During Li⁺ deintercalation, the opposite phenomenon occurs, starting with the C2 capacitive region covering the −0.6–0.4 V versus Ag/Ag⁺ potential range during the anodic cycle. Then, the current peak emerges at around 0.5 V versus Ag/Ag⁺. Notably, those current peaks in both charge and discharge have been attributed to surface-controlled partial charge transfer involving the intercalation/deintercalation of solvated Li⁺ cations, contributing to the increased capacity in the WIS electrolyte.[29,39,42] Following the oxidation current peak, symmetrically to what has been seen in charge, the current decreases when entering the C1 region between 0.6 and 0.75 V versus Ag/Ag⁺.

This study employed various *operando* techniques on this system to delve deeper into the charging–discharging mechanisms within each region (**Figure** 2a,b,c).

The CVs corresponding to each measurement are reported in Figure S2 (Supporting Information). Figure 2a,b,c shows the in-plane resistance variation of a $Ti_3C_2T_x$ free-standing film, the thickness variation (displacement along the *z*-axis, directly related to interlayer space changes) obtained through ECD on a $Ti_3C_2T_x$ free-standing film, and the mass variation obtained by EQCM-A with freeze-dried $Ti_3C_2T_x$ powder sprayed on a 9 MHz quartz, respectively (details in the Experimental Section).

Starting from the fully discharged state (black squares in Figure 2a,b,c) and starting cathodic polarization (charging), the resistance initially exhibits a slight decrease as the system goes through the C1 region (Figure 2a). Conversely, the dilatometry

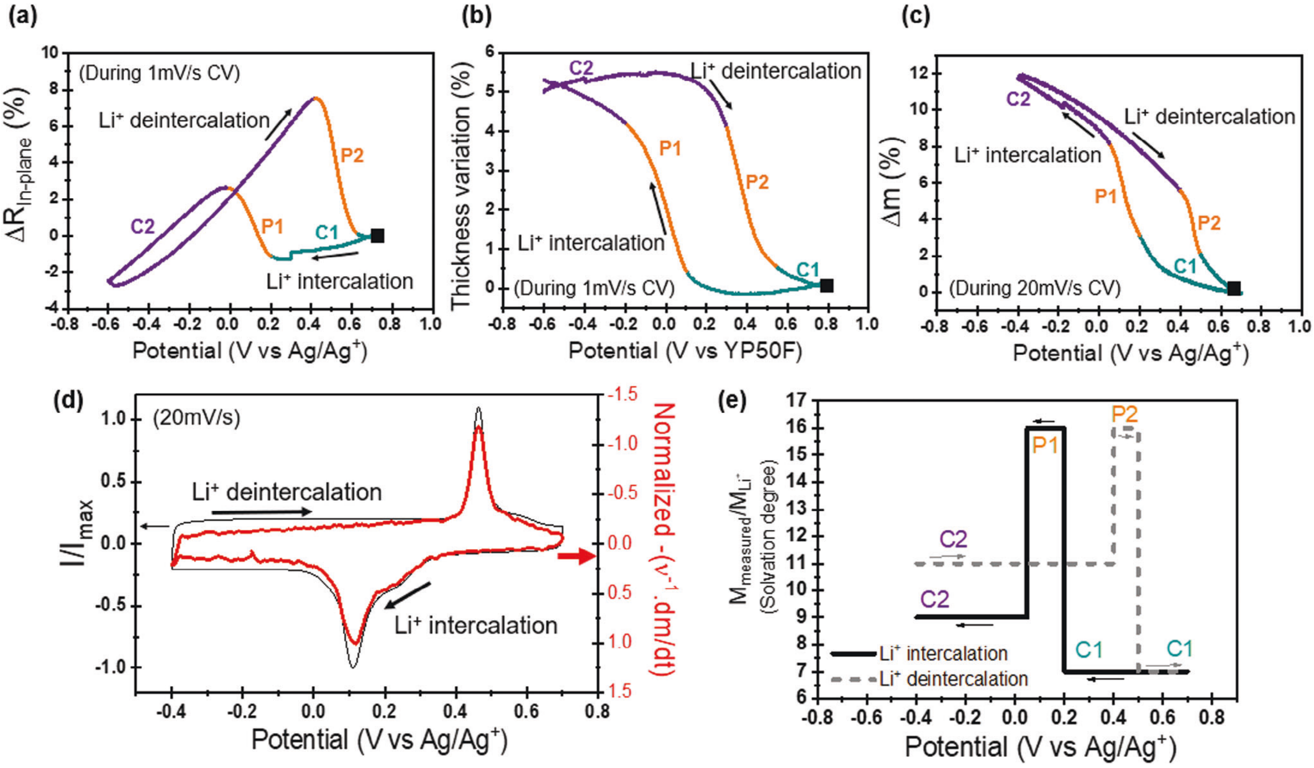

Figure 2. *Operando* a) in-plane resistance, b) thickness, and c) mass flux measurement of $Ti_3C_2T_x$ in the 20 M LiCl water-in-salt electrolyte during cyclic voltammetry. The black squares indicate the fully delithiated state, used as starting points for analysis. d) Normalized current (left y-axis) and normalized mass flux (right y-axis) versus the potential obtained through EQCM-A (associated with the results shown in (c)). e) Solvation degree versus the potential, obtained through EQCM-A molar masses calculation (associated with the results shown in (c).

measurement reveals no thickness variation within this region (Figure 2b), consistent with the XRD findings indicating no interlayer distance variation within this initial capacitive area of the CV (Figure S3, Supporting Information).[29] This observation also aligns well with the EQCM-D results from Wang et al.,[29] showing that the Li^+ ions, entering without a solvation shell in this potential region, do not affect the interlayer distance. Consequently, no ECD thickness variation is expected.

It is worth mentioning that, overall, the resistance of the $Ti_3C_2T_x$ electrode is affected by two primary factors: intrasheet resistance, which is sensitive to charge carrier density or mobility variations, and inter-sheet resistance, which is related to interlayer spacing and intercalated species.[43] As the electronic charge carrier mobility has already been reported as independent of the applied potential, the intrasheet conductivity was solely attributed to charge carrier density in this study.[27] Thus, the resistance variation recorded in the C1 region during charge, since not related to the thickness or interlayer distance variation, is most probably associated with an intrasheet resistance decrease linked to charge carrier density variation (density of state change).[40,43–45]

Upon entering the P1 region, the resistance undergoes a sharp increase (Figure 2a), coinciding with an abrupt thickness augmentation (Figure 2b), also consistent with the recorded interlayer spacing increase.[29] Notably, these results align with previous findings on $Ti_3C_2T_x$ in an aqueous acidic electrolyte, where a correlation was found between interlayer spacing and in-plane resistance of $Ti_3C_2T_x$.[40] Interestingly, during further Li^+ ions insertion, a significant linear decrease in resistance occurs within the C2 region. However, no substantial thickness variation is recorded in this area (Figure 2b), and no interlayer space variation was reported.[29]

The EQCM-A data in Figure 2c shows a mass intake throughout the charging process. Moreover, a change in slope can be observed within the P1 region, indicating an enhanced mass flux during the intercalation of solvated Li^+ ions. This observation is further supported by Figure 2d, which reveals minor mass flux variation within C1 and C2 regions, and that the maximums of the current and mass flux are well-aligned at the current peak potential (P1 and P2 regions, current and mass flux are normalized with the maximum cathodic values, v being the scan rate). Symmetrically, at the beginning of discharge (C2), no change in thickness is observed (Figure 2b), while a sharp increase in resistance is recorded in this capacitive region (Figure 2a). Subsequently, a consequent resistance and thickness decrease happens during P2, mirroring the trend observed during cations intercalation (Figure 2a,b). Finally, within the C1 region, both resistance and thickness stabilize (Figure 2a,b). Overall, in both charge and discharge, the thickness variations recorded by ECD are consistent with atomic force microscopy results obtained by Wang et al.[29] Interestingly, the linear resistance variation recorded in the C2 region, greater than the one recorded in C1, occurs while no interlayer distance variation happens,[29] and no significant thickness variation is observed (ECD plot, Figure 2b)—only 1% over the total 6% variation. This resistance variation is probably due to an intrasheet resistance decrease linked to charge carrier density variation (density of state change).[40,43–45] In addition, considering the layered structure of the $Ti_3C_2T_x$ MXene electrode, this resistance decrease may also stem from a diminished tunneling energy barrier (inter-sheet resistance decrease) due to the increased presence of Li^+ ions between the sheets.[43] Notably, the CV data (Figure 1a) shows that the capacitive current is higher in C2 than in C1. During charge, since the thickness growth is relatively modest following P1, and the interlayer spacing already had undergone a sharp increase during P1 (reduction peak), compared to the initial state, one can assume that the system reached an expanded state after P1, facilitating the entry of more Li^+ ions compared to the C1 state, thus enhancing the capacitive performance (double layer charge). Regarding EQCM-A measurements (Figure 2c), a mass decrease is observed throughout the entire delithiation process, as for the lithium intercalation process. Three distinct regions can be spotted, corresponding to the previously described areas C2, P2, and C1.

In a previous report, Wang et al. demonstrated through EQCM with Dissipation monitoring (EQCM-D) that the three stages outlined previously are correlated with different solvation numbers of the Li^+ ions being intercalated/deintercalated.[29,39] Within the C1 region, almost no water accompanies the inserting cation. Conversely, in the current peak regions (P1 and P2), the amount of water entering with the cation increases, eventually reaching the hydration number of Li^+ ions in the bulk of the WIS electrolyte (2.85 water molecules per intercalated Li^+ ion). In the subsequent C2 region, the number of solvating water molecules decreases, reaching the hydration number of Li^+ ions in a diluted SIW electrolyte (1.45 water molecules per Li^+ ion). The molecular weight of the adsorbed species can be extracted from the presented EQCM-A data (details in the Experimental Procedures and Supporting Information). Given that the cation flux is strongly favored due to the negatively charged $Ti_3C_2T_x$ surface and the polarization toward more negative potentials (resulting in an elevated concentration of cations in the immediate vicinity of the $Ti_3C_2T_x$ surface), the type of adsorbed species is expected to be $Li^+ + xH_2O$, with x being determined by analysis of the mass-to-charge charge plot from EQCM-A data. The determined molar masses are given in the Supporting Information. Figure 2e shows the degree of solvation, defined as the measured molar mass divided by the molar mass of lithium (see the Experimental Section), versus the CV potential. It is observed that there are more water molecules accompanying Li^+ ion intercalation in the current peak regions, and more water molecules entering with the cation in the low potential capacitive area (C2) compared to the high potential capacitive region (C1). This trend agrees with the previous EQCM-D, XRD, and FTIR results on this system (Figure S3, Supporting Information).[29,39]

2.2. $Ti_3C_2T_x$ in the SIW Electrolyte

To investigate the charge storage processes further, particularly in the C2 region, we conducted the same characterizations in a regular SIW electrolyte, specifically 1 M LiCl. The CV normalized to the absolute value of the maximum cathodic current (measured in the in-plane cell, see the Experimental Procedures Section) along with the dimensionless charge versus potential plots are presented in **Figure 3**a,b, respectively. In contrast to the behavior observed in the WIS electrolyte, the charge storage mechanism in this electrolyte is entirely capacitive, as evidenced by the rectangular voltammogram (Figure 3a) and the linear relationship between charge and potential (Figure 3b).

Figure 4a,b,c below depicts the results obtained from the *operando* techniques. Figure 4a illustrates the *operando* in-plane resistance measurement, Figure 4b exhibits the *operando* thickness variation obtained by ECD, with the same scale as Figure 2b, and Figure 4c shows the *operando* electrode mass variation acquired through EQCM-A. The CVs corresponding to each measurement for $Ti_3C_2T_x$ in SIW LiCl are reported in Figure S4 (Supporting Information).

Figure 4a illustrates that the resistance decreases linearly from 0.2 to −0.9 V versus Ag/Ag^+ upon Li^+ ions intercalation, followed by a linear increase as the system discharges. At the end of discharge, from −0.2 to 0.2 V versus Ag/Ag^+, the speed of resistance increase is reduced, and resistance reaches a plateau. The thickness variation (Figure 4b) is 6 times smaller than recorded in the WIS electrolyte (−0.6% in the SIW against 5.5% in the WIS electrolyte). Moreover, a slight thickness decrease is noticeable at low potentials, consistent with the reduction in interlayer distance observed in Li-based diluted aqueous electrolytes, attributed to the screening effect arising from the presence of Li^+ ions between the sheet, reducing the repulsion between negatively charged MXene layers.[30,46] Such a small thickness variation in the SIW electrolyte upon cycling is consistent with a capacitive charge storage mechanism.

EQCM-A measurement in Figure 4c shows a monotonous mass intake during Li^+ ions intercalation and a corresponding decrease during Li^+ ions deintercalation until −0.3 V versus Ag/Ag^+. The extracted equivalent molar mass is 158 g mol^{-1}, corresponding to the intercalation/deintercalation of $Li^+ + 8\ H_2O$. As expected, this is higher than measured in the WIS electrolyte because of the higher number of free water molecules able to intercalate with the cation in the SIW electrolyte.

The observed resistance variation may be attributed to interlayer distance variation, resulting from slight thickness changes, as previously reported,[40] where intersheet conductivity increases when interlayer space decreases. Additionally, increased charge carrier density and reduced intersheet hopping energy, as explained earlier for the C2 region in the WIS electrolyte, might also contribute to the resistance change.

2.3. WIS/SIW Comparison

In general, our findings further emphasize that an active material's behavior is dictated not only by its intrinsic properties but also by its interplay with the selected electrolyte. Indeed, the $Ti_3C_2T_x$ MXene exhibits different charging and discharging mechanisms depending on the LiCl concentration.

Regarding $Ti_3C_2T_x$ in the WIS LiCl, a small initial decrease in resistance in region C1 during cation intercalation happens, probably due to an intrasheet conductivity augmentation, considering the absence of any thickness change of the MXene electrode. In the P1 region, when the current peak related to the

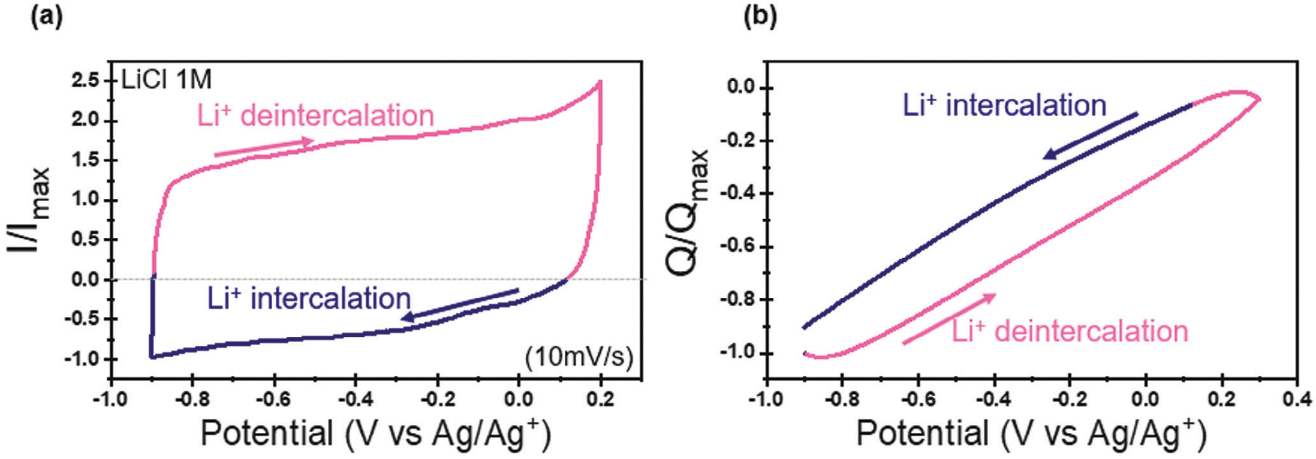

Figure 3. a) Cyclic voltammetry of a $Ti_3C_2T_x$ freestanding film at 10 mV s^{-1}, in 1 м LiCl, performed in the in-plane resistance measurement cell. The current is normalized to the absolute maximum cathodic value. b) Normalized charge plotted versus potential, calculated from the CV displayed in (a). The charge is normalized to the maximum value.

adsorption of solvated cation appears, a significant increase in electrode thickness occurs, leading to a rise of intersheet resistance. In region C2, similar to what can be seen in C1, the increase in the charge carrier density causes a decrease in intrasheet resistance. A reduced tunneling energy barrier (intersheet resistance) can also be a reason for this resistance decrease. The greater resistance variation recorded in C2 aligns with this region's higher current and higher capacity, indicating that storing more ions and more injected counter charges increases the intrasheet conductivity.

In the case of $Ti_3C_2T_x$ in the SIW LiCl electrolyte, the insertion of the Li^+ ion and its solvation shell does not cause any electrode swelling upon polarization. This suggests that the electrode was already irreversibly expanded along the *z*-axis after immersion in the electrolyte, with sufficient interlayer spacing to accommodate the Li^+ ions and the water molecules. Indeed, previous results have shown a spontaneous increase of interlayer distance at open circuit voltage (OCV) following $Ti_3C_2T_x$ MXene immersion in 1 м LiCl electrolyte, higher than recorded in the corresponding WIS electrolyte.[30] The small thickness variation recorded in the 1 м LiCl electrolyte observed here could thus be explained by a facilitated capacitive charge storage mechanism following the spontaneous insertion of water molecules and solvated ions between the MXene layers directly after immersion in the electrolyte. This claim is confirmed by in-plane electrochemical impedance spectroscopy (EIS) measurement at OCV, achieved at different impregnation times, as presented in Figure S5 (Supporting Information). The in-plane impedance of the $Ti_3C_2T_x$ electrode at OCV being sensitive to interlayer space variation (intersheet resistance), electrode impregnation with electrolyte at OCV should thus lead to a variation of the interlayer distance and directly affect the electrode impedance.[40] Figure S5 (Supporting Information) clearly shows that while only very small impedance variations have been recorded (+1.77%) upon electrode immersion in the WIS LiCl electrolyte, much higher variations (+131%) are recorded in the SIW LiCl electrolyte. These results are also supported by contact angle measurements presented in Figure S6 (Supporting Information), which indicate that the WIS electrolyte, due to higher concentration and consequently greater viscosity, reduces wetting of the $Ti_3C_2T_x$ surface compared to the more diluted SIW electrolyte. As a result, the WIS electrolyte does not spontaneously enter within the MXene layers at OCV. During further lithium intercalation, a slight shrinkage of the electrode is observed, contrary to the behavior observed in WIS LiCl.

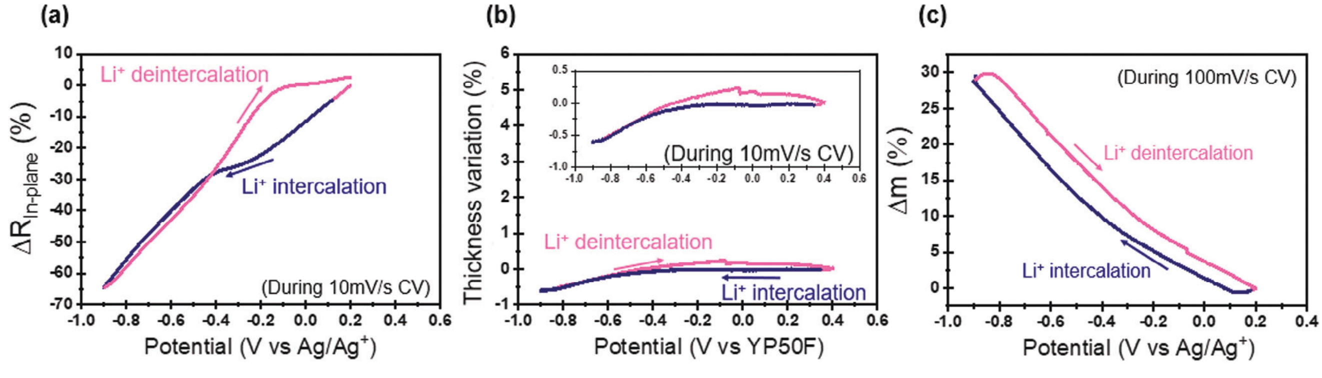

Figure 4. *Operando* a) in-plane resistance, b) thickness, and c) mass flux measurement of $Ti_3C_2T_x$ in the 1 м LiCl salt-in-water electrolyte during cyclic voltammetry.

The positively charged Li ions act as screens, diminishing repulsive forces between the negatively charged MXene sheet.[29,33] The reduction in electrode thickness during Li^+ ions intercalation (interlayer spacing decrease) leads to an increase in intersheet conductivity. Additionally, as observed for the C2 region in WIS LiCl, polarization toward more negative potentials increases charge carrier density, further decreasing the resistance. This behavior has also been observed with carbon material in aqueous electrolytes.[40] A reduced intersheet electron hopping energy barrier, and thus intersheet resistance, can also not be ruled out. Both intra- and intersheet conductivity may decrease, contributing to the recorded resistance decrease upon Li^+ ion intercalation.

3. Conclusion

The utilization of diverse and powerful *operando* techniques has elucidated the varying physical properties of $Ti_3C_2T_x$ upon cations intercalation/deintercalation in WIS and SIW LiCl electrolytes. These findings underscore further that the electrochemical behavior of an active material is influenced not only by its intrinsic properties but also by its interplay with the electrolyte.

In the WIS electrolyte, the in-plane resistance measurement of $Ti_3C_2T_x$ revealed variations linked to the thickness changes, with an increase in intersheet resistance when the interlayer space is increased. Besides, unrelated to any thickness variation, a linear resistance decrease/increase was observed in the low potential capacitive region during charging/discharging. This is attributed to the variation in charge carrier density (intrasheet resistance variation) or a reduced electron hopping energy barrier between $Ti_3C_2T_x$ sheets due to the increased Li^+ ions concentration between the MXene layers (intersheet resistance variation). Conversely, in the SIW electrolyte, the resistance exhibited a monotonous decrease/increase during charging/discharging, while only slight thickness variations were recorded upon Li^+ ions intercalation/deintercalation. Similar to capacitive regions of $Ti_3C_2T_x$ in WIS electrolyte, this may be due to either charge carriers' density variation or a reduced intersheet electron tunneling energy barrier. The thickness variations obtained by ECD agree with the microscale variation of the interlayer spacing measured by XRD. EQCM-A measurements are in accordance with the findings for the WIS electrolyte reported in the literature, confirming the solvated Li^+ ions intercalation at the current peak potential. The larger number of water molecules accompanying lithium ions in the low-potential capacitive area further confirmed an "activation-deactivation" mechanism at the current peak, leading to increased capacity and interlayer spacing and, thus, reduced desolvation of the lithium upon entry between the MXene sheets. In the SIW electrolyte, almost no thickness change was observed upon polarization, but an irreversible change was recorded at OCV, as suggested by the large electrode impedance variation recorded immediately after immersion of the $Ti_3C_2T_x$ electrode in the electrolyte. EQCM-A shows that Li^+ ions enter with their full solvation shell, implying sufficient interlayer space after immersion in the electrolyte to accommodate solvated lithium and the solvent molecules.

Overall, these results provide a comprehensive understanding of the variations of the physical properties of the $Ti_3C_2T_x$ MXene upon lithium intercalation/deintercalation in WIS and SIW aqueous electrolytes with the combination of different characterization techniques. In the context of growing interest in *operando* techniques, this work illustrates how integrating such versatile and powerful tools can help understand the charge/discharge mechanisms in MXenes and other materials for energy storage.[40,47–53]

4. Experimental Section

For all electrochemical experimentation, the used electrolytes are 20 м LiCl (WIS) or 1 м LiCl (SIW) in water. Molality (m) has been used instead of molarity (M) for the WIS electrolyte to account for the volume variation of the solution after the addition of the large quantity of salt (20 m is thus 20 moles of salt per liter of solvent, whereas 1 м is a mole of salt per liter of solution).

Material Synthesis: $Ti_3C_2T_x$ was synthesized by etching the corresponding MAX phases (325 mesh, Ti_3AlC_2) with a mixture of HF (48.5%–51%, Acros Organics) and HCl (36.5%–38%, Fisher Chemical) acids. Typically, 1 g of Ti_3AlC_2 powder was added to 2 mL of HF, 12 mL of HCl, and 6 mL of De-Ionized (DI) water. The mixture was stirred at 35 °C for 1 day. After etching, the reacted solution was repeatedly washed with DI water through centrifugation at 3500 rpm for 5 min until the pH was > 6. After washing, the sediment was dispersed in a mixture of 10 mL DI water and 1 g of LiCl for stirring overnight. After that, the mixture was washed repeatedly with DI water by centrifugation at 10 000 rpm for 5 min until the pH was <8. At last, the supernatant was collected as MXene solutions after centrifugation at 3500 rpm for 10 min.

Vacuum-Filtered MXene Electrode Preparation: The freestanding MXene films were prepared by vacuum-assisted filtration of the colloidal MXene dispersion on a polypropylene membrane with a thickness of 25 µm (3501 Coated PP, Celgard LLC) followed by vacuum drying.

In-Plane Resistance and Impedance Measurements: *Operando* in-plane resistance measurements were performed with a potentiostat/galvanostat from Gamry Instruments (potentiostat #2 in Figure S1, Supporting Information). The changes in the in-plane resistance of the electrode upon cycling (potentiostat #1 in Figure S1 (Supporting Information), Biologic or Gamry Instruments) were measured using the complete electrochemical setup depicted in Figure S1 (Supporting Information), utilizing the two potentiostats. Potentiostat #2 was used to apply a small current (I_{CP} = 10 mA) while recording the voltage drop DV_{CP} (V) during the cycling of the sample through potentiostat #1 to allow accessing the DC resistance $R_{in-plane}$ (Ω) through Ohm's law (Equation (1))

$$R_{in-plane} = \frac{\Delta V_{CP}}{I_{CP}} \tag{1}$$

The resistance variation $\Delta R_{in-plane}$ (%) was then calculated thanks to Equation (2) below, with R_0 the initial resistance (Ω) of the fully discharged material

$$\Delta R_{in-plane} = \frac{R_{in-plane} - R_0}{R_0} \times 100 \tag{2}$$

The CV scans were performed at 1 and 10 mV s^{-1} for 20 m and 1 м LiCl solutions, respectively, to reduce ohmic drop coming from the setup and to match the scan rate used in dilatometry cell. The working electrode was a $Ti_3C_2T_x$ free-standing film obtained by vacuum-assisted filtration with a thickness of around 5–8 µm. The counter electrode was an overcapacitive activated carbon film, and the reference electrode was a silver wire. The measurement was performed during several cycles to ensure the system was stabilized, and a representative cycle was then chosen for the figure.

Electrochemical Quartz Microbalance: EQCM-A experiments were performed using a SEIKO EG&G QCM922A to record the frequency change during electrochemical cycling performed with a Biologic potentiostat. Freeze-dried $Ti_3C_2T_x$ powder was dispersed in water and spray-coated on

9 MHz Ti/Au quartz sensors (AWSensors). Faster scan rates of 20 and 100 mV s^{-1} in 20 m and 1 м LiCl were possible and preferred in EQCM because of the small mass of active material enhancing surface reactivity at a low scan rate. The WIS system displays redox-like features; it was, however, necessary to reduce the scan rate compared to the purely capacitive WIS system. Mass loadings were deduced from the frequency change in the air and were 52 µg cm^{-2} for 20 м LiCl and 15 µg cm^{-2} for 1 м LiCl. The frequency variations Δf (Hz) were converted into mass variations, $\Delta m_{\text{Sauerbrey}}$ (g), using the Sauerbrey equation (Equation (3)), valid for stiff films[54]

$$\Delta m_{\text{Sauerbrey}} = -\frac{\sqrt{\rho_q \mu_q}}{2f_0^2} \Delta f \tag{3}$$

where ρ_q is the quartz density (g cm^{-3}), μ_q is the quartz shear modulus (g cm^{-1} s^{-2}), and f_0 is the quartz fundamental frequency (Hz). The percentage mass variation Δm (%) values plotted in Figures 2c, 5c; and Figures S2c and S4c were obtained using Equation (4) below, where m_0 is the mass of material sprayed on the quartz (µg)

$$\Delta m = \frac{\Delta m_{\text{Sauerbrey}}}{m_0} \times 100 \tag{4}$$

Eventually, it is possible to extract molecular weights of the adsorbed species from EQCM data by plotting the charge versus the mass change. The slope of this plot can give access to molar mass thanks to Sauerbrey and Faraday's first law of electrolysis equations, only if the frequency variations are solely caused by electrode weight variations (elastic behavior). The motional resistance is plotted versus frequency change in Figure S7 (Supporting Information), illustrating the elastic behavior of the coating and, thus, the possibility to extract molecular weight thanks to Equation (5) using the slope of the Δm versus ΔQ curve

$$M = \frac{m}{Q} \times \text{nF} \tag{5}$$

where M is the atomic mass of the specie (g mol^{-1}), $\frac{m(\text{g})}{Q(\text{C})}$ is the slope of the Δm versus ΔQ plot, n is the number of transferred electrons, and F the Faraday constant (C mol^{-1}). The degree of solvation discussed in the main text was calculated by dividing the calculated molar mass by the molar mass of Lithium.

For EQCM experiments, the counter electrode was a carbon electrode, and the reference electrode was a silver wire. 10 and 50 mV s^{-1} scan rates were used for 20 m and 1 м LiCl, respectively. The measurement was performed during several cycles to ensure the system was stabilized, and a representative cycle was then chosen for the figure.

Dilatometry: ECD experiments were performed with an EL-CELL ECD-3-nano dilatometer (5 nm resolution) during electrochemical cycling with a Biologic potentiostat. Vacuum-filtered free-standing $Ti_3C_2T_x$ films of about 8–5 µm thickness were used as working electrodes. Counter and reference electrodes were both made of carbon. A stiff porous frit separates the counter and working electrodes in the ECD cell, allowing only the working electrode thickness changes to be transmitted to a capacitive displacement sensor. A slow scan rate of 1 or 10 mV s^{-1} is needed for ECD measurements to reduce the ohmic drop coming from the resistance of the ECD cell. ECD data shown in this paper are averaged data from several cycles, corrected from the displacement drift induced by the cell. The recorded sensor position was converted into thickness variation (%) using Equation (6) below

$$\text{Thicknes variation} \quad (\%) = \frac{z - z_0}{e} \tag{6}$$

where z is the sensor position (µm), z_0 is the initial position at the fully discharged state (µm), and e is the thickness of the electrode (µm).

Considering the 2D structure of $Ti_3C_2T_x$ and the prominent variation of the *c*-lattice parameter as compared to the *a* and *b* parameters, the displacement of the sensor along the *z*-axis is assimilated in the text to a *c*-lattice-parameter-related thickness variation of the vacuum-filtered MXene electrode.[46]

Supporting Information

Supporting Information is available from the Wiley Online Library or from the author.

Acknowledgements

D.Z., R.W., and Y.G. acknowledged funding for MXene synthesis from NSF Grant No. DMR-2041050. P.S. acknowledged the support from the ERC (MoMa-STOR Synergy Grant No. 951513) and the LABEX STOREX of the Agence Nationale de la Recherche. A.P. was supported by the ERC (MoMa-STOR Synergy Grant No. 951513). P.S. and P.L.T. acknowledged the support of the PEPR Batteries ANR-22-PEBA-0003. P.S., P.L.T., and Y.G. designed the research plan. A.P. and D.Z. conducted the experiments. All authors contributed to the discussion and preparation of the manuscript.

Conflict of Interest

The authors declare no conflict of interest.

Data Availability Statement

The data that support the findings of this study are available from the corresponding author upon reasonable request.

Keywords

conductivity, dilatometry, EQCM, in-plane resistance, MXene, *operando* techniques, titanium carbide

Received: October 28, 2024
Revised: January 14, 2025
Published online:

---

[1] A. VahidMohammadi, J. Rosen, Y. Gogotsi, *Science* **2021**, *372*, eabf1581.
[2] V. Kamysbayev, A. S. Filatov, H. Hu, X. Rui, F. Lagunas, D. Wang, R. F. Klie, D. V. Talapin, *Science* **2020**, *369*, 979.
[3] A. Lipatov, M. Alhabeb, H. Lu, S. Zhao, M. J. Loes, N. S. Vorobeva, Y. Dall'Agnese, Y. Gao, A. Gruverman, Y. Gogotsi, A. Sinitskii, *Adv. Elect. Mater.* **2020**, *6*, 1901382.
[4] C. Ma, M. Ma, C. Si, X. Ji, P. Wan, *Adv. Funct. Mater.* **2021**, *31*, 2009524.
[5] Z. Ling, C. E. Ren, M.-Q. Zhao, J. Yang, J. M. Giammarco, J. Qiu, M. W. Barsoum, Y. Gogotsi, *Proc. Natl. Acad. Sci. USA* **2014**, *111*, 16676.
[6] Y. Gogotsi, *Chem. Mater.* **2023**, *35*, 8767.
[7] M. Naguib, M. Kurtoglu, V. Presser, J. Lu, J. Niu, M. Heon, L. Hultman, Y. Gogotsi, M. W. Barsoum, *Adv. Mater.* **2011**, *23*, 4248.
[8] T. S. Mathis, K. Maleski, A. Goad, A. Sarycheva, M. Anayee, A. C. Foucher, K. Hantanasirisakul, C. E. Shuck, E. A. Stach, Y. Gogotsi, *ACS Nano* **2021**, *15*, 6420.
[9] J. Zhang, N. Kong, S. Uzun, A. Levitt, S. Seyedin, P. A. Lynch, S. Qin, M. Han, W. Yang, J. Liu, X. Wang, Y. Gogotsi, J. M. Razal, *Adv. Mater.* **2020**, *32*, 2001093.

[10] M. Downes, C. E. Shuck, B. McBride, J. Busa, Y. Gogotsi, *Nat. Protoc.* **2024**, *19*, 1807.
[11] B. Anasori, M. R. Lukatskaya, Y. Gogotsi, *Nat. Rev. Mater.* **2017**, *2*, 16098.
[12] Q. Zhu, J. Li, P. Simon, B. Xu, *Energy Storage Mater.* **2021**, *35*, 630.
[13] J. Zhao, Q. Li, T. Shang, F. Wang, J. Zhang, C. Geng, Z. Wu, Y. Deng, W. Zhang, Y. Tao, Q.-H. Yang, *Nano Energy* **2021**, *86*, 106091.
[14] C.-H. Wang, N. Kurra, M. Alhabeb, J.-K. Chang, H. N. Alshareef, Y. Gogotsi, *ACS Omega* **2018**, *3*, 12489.
[15] F. Malchik, N. Shpigel, M. D. Levi, T. R. Penki, B. Gavriel, G. Bergman, M. Turgeman, D. Aurbach, Y. Gogotsi, *Nano Energy* **2021**, *79*, 105433.
[16] D. Pang, M. Alhabeb, X. Mu, Y. Dall'Agnese, Y. Gogotsi, Y. Gao, *Nano Lett.* **2019**, *19*, 7443.
[17] V. H. Nguyen, R. Tabassian, S. Oh, S. Nam, M. Mahato, P. Thangasamy, A. Rajabi-Abhari, W. Hwang, A. K. Taseer, I. Oh, *Adv. Funct. Mater.* **2020**, *30*, 1909504.
[18] F. Shahzad, M. Alhabeb, C. B. Hatter, B. Anasori, S. M. Hong, C. M. Koo, Y. Gogotsi, *Science* **2016**, *353*, 1137.
[19] M. Han, C. E. Shuck, R. Rakhmanov, D. Parchment, B. Anasori, C. M. Koo, G. Friedman, Y. Gogotsi, *ACS Nano* **2020**, *14*, 5008.
[20] T. Yun, H. Kim, A. Iqbal, Y. S. Cho, G. S. Lee, M. Kim, S. J. Kim, D. Kim, Y. Gogotsi, S. O. Kim, C. M. Koo, *Adv. Mater.* **2020**, *32*, 1906769.
[21] X. Han, J. Huang, H. Lin, Z. Wang, P. Li, Y. Chen, *Adv. Healthcare Mater.* **2018**, *7*, 1701394.
[22] N. Driscoll, B. Erickson, B. B. Murphy, A. G. Richardson, G. Robbins, N. V. Apollo, G. Mentzelopoulos, T. Mathis, K. Hantanasirisakul, P. Bagga, S. E. Gullbrand, M. Sergison, R. Reddy, J. A. Wolf, H. I. Chen, T. H. Lucas, T. R. Dillingham, K. A. Davis, Y. Gogotsi, J. D. Medaglia, F. Vitale, *Sci. Transl. Med.* **2021**, *13*, eabf8629.
[23] F. Meng, M. Seredych, C. Chen, V. Gura, S. Mikhalovsky, S. Sandeman, G. Ingavle, T. Ozulumba, L. Miao, B. Anasori, Y. Gogotsi, *ACS Nano* **2018**, *12*, 10518.
[24] C. Zhan, M. Naguib, M. Lukatskaya, P. R. C. Kent, Y. Gogotsi, D. Jiang, *J. Phys. Chem. Lett.* **2018**, *9*, 1223.
[25] X. Mu, D. Wang, F. Du, G. Chen, C. Wang, Y. Wei, Y. Gogotsi, Y. Gao, Y. Dall'Agnese, *Adv. Funct. Mater.* **2019**, *29*, 1902953.
[26] M. R. Lukatskaya, O. Mashtalir, C. E. Ren, Y. Dall'Agnese, P. Rozier, P. L. Taberna, M. Naguib, P. Simon, M. W. Barsoum, Y. Gogotsi, *Science* **2013**, *341*, 1502.
[27] M. D. Levi, M. R. Lukatskaya, S. Sigalov, M. Beidaghi, N. Shpigel, L. Daikhin, D. Aurbach, M. W. Barsoum, Y. Gogotsi, *Adv. Energy Mater.* **2015**, *5*, 1400815.
[28] Z. Lin, P. Rozier, B. Duployer, P.-L. Taberna, B. Anasori, Y. Gogotsi, P. Simon, *Electrochem. Commun.* **2016**, *72*, 50.
[29] X. Wang, T. S. Mathis, Y. Sun, W.-Y. Tsai, N. Shpigel, H. Shao, D. Zhang, K. Hantanasirisakul, F. Malchik, N. Balke, D. Jiang, P. Simon, Y. Gogotsi, *ACS Nano* **2021**, *15*, 15274.
[30] Y. Zhu, S. Zheng, P. Lu, J. Ma, P. Das, F. Su, H.-M. Cheng, Z.-S. Wu, *Natl. Sci. Rev.* **2022**, *9*, nwac024.
[31] K. Kim, Y. Ando, A. Sugahara, S. Ko, Y. Yamada, M. Otani, M. Okubo, A. Yamada, *Chem. Mater.* **2019**, *31*, 5190.
[32] K. Kim, M. Okubo, A. Yamada, *J. Electrochem. Soc.* **2019**, *166*, A3739.
[33] N. Shpigel, A. Chakraborty, F. Malchik, G. Bergman, A. Nimkar, B. Gavriel, M. Turgeman, C. N. Hong, M. R. Lukatskaya, M. D. Levi, Y. Gogotsi, D. T. Major, D. Aurbach, *J. Am. Chem. Soc.* **2021**, *143*, 12552.
[34] Y. Li, J. Chen, P. Cai, Z. Wen, *J. Mater. Chem. A* **2018**, *6*, 4948.
[35] A. Bunpheng, P. Sakulaue, W. Hirunpinyopas, K. Nueangnoraj, S. Luanwuthi, P. Iamprasertkun, *J. Electroanal. Chem.* **2023**, *944*, 117645.
[36] Y. Zhu, Q. Zhang, J. Ma, P. Das, L. Zhang, H. Liu, S. Wang, H. Li, Z. Wu, *Carbon Energy* **2024**, *6*, e481.
[37] Y. Zhu, S. Zheng, J. Qin, J. Ma, P. Das, F. Zhou, Z.-S. Wu, *Fundament. Res.* **2024**, *4*, 307.
[38] Y. Zhu, J. Ma, P. Das, S. Wang, Z. Wu, *Small Methods* **2023**, *7*, 2201609.
[39] M. Lounasvuori, T. S. Mathis, Y. Gogotsi, T. Petit, *J. Phys. Chem. Lett.* **2023**, *14*, 1578.
[40] V. Maurel, K. Brousse, T. S. Mathis, A. Perju, P.-L. Taberna, P. Simon, *J. Electrochem. Soc.* **2022**, *169*, 120510.
[41] A. Perju, B. Mondal, V. Maurel, F. Rabuel, M. Morcrette, P.-L. Taberna, P. Simon, *J. Electrochem. Soc.* **2024**, *171*, 110511.
[42] D. Zhang, R. Wang, X. Wang, Y. Gogotsi, *Nat. Energy* **2023**, *8*, 567.
[43] J. L. Hart, K. Hantanasirisakul, A. C. Lang, B. Anasori, D. Pinto, Y. Pivak, J. T. Van Omme, S. J. May, Y. Gogotsi, M. L. Taheri, *Nat. Commun.* **2019**, *10*, 522.
[44] E. Pollak, I. Genish, G. Salitra, A. Soffer, L. Klein, D. Aurbach, *J. Phys. Chem. B* **2006**, *110*, 7443.
[45] E. Pollak, A. Anderson, G. Salitra, A. Soffer, D. Aurbach, *J. Electroanal. Chem.* **2007**, *601*, 47.
[46] J. Come, J. M. Black, M. R. Lukatskaya, M. Naguib, M. Beidaghi, A. J. Rondinone, S. V. Kalinin, D. J. Wesolowski, Y. Gogotsi, N. Balke, *Nano Energy* **2015**, *17*, 27.
[47] J. Miranda, G. Franklin, T. S. Mathis, P.-L. Taberna, P. Simon, *Energy Storage Mater.* **2024**, *65*, 103105.
[48] D. Liu, Z. Shadike, R. Lin, K. Qian, H. Li, K. Li, S. Wang, Q. Yu, M. Liu, S. Ganapathy, X. Qin, Q. Yang, M. Wagemaker, F. Kang, X. Yang, B. Li, *Adv. Mater.* **2019**, *31*, 1806620.
[49] C. Villevieille, T. Sasaki, P. Novák, *RSC Adv.* **2014**, *4*, 6782.
[50] K. Fic, A. Płatek, J. Piwek, J. Menzel, A. Ślesiński, P. Bujewska, P. Galek, E. Frąckowiak, *Energy Storage Mater.* **2019**, *22*, 1.
[51] F. Strauss, D. Kitsche, Y. Ma, J. H. Teo, D. Goonetilleke, J. Janek, M. Bianchini, T. Brezesinski, *Adv. Energy Sustainable Res.* **2021**, *2*, 2100004.
[52] J. Huang, L. Albero Blanquer, J. Bonefacino, E. R. Logan, D. Alves Dalla Corte, C. Delacourt, B. M. Gallant, S. T. Boles, J. R. Dahn, H.-Y. Tam, J.-M. Tarascon, *Nat. Energy* **2020**, *5*, 674.
[53] W.-Y. Tsai, P.-L. Taberna, P. Simon, *J. Am. Chem. Soc.* **2014**, *136*, 8722.
[54] G. Sauerbrey, *European Physical Journal* **1959**, *155*, 206.